ACS APPLIED POLYMER MATERIALS

pubs.acs.org/acsapm Article

Transparent Polyimide Aerogels: Controlled Porosity via Minimizing the Phase Separation

Magi Y. Mettry,* Ariel M. Lighty, Joshua A. Hammons, Daniel R. Malone, Kaila M. Bertsch, and Tyler M. Fears

Cite This: https://doi.org/10.1021/acsapm.2c00957 Read Online

ABSTRACT: The aerogels industry has been growing with a market capacity of 909 billion USD in 2019. Silica aerogels are the most extensively used due to their ease of synthesis. It can possess many useful properties such as high optical transparency, high-surface area, low thermal conductivity, and a wide accessible density range. However, silica aerogels are brittle and friable, making them unsuitable for many applications. Polymeric aerogels are typically much more robust but lack the uniform fine nanostructure which gives silica its exceptional properties. Herein, mechanically robust polyimide (PI) aerogels with uniform <20 nm porosity and exceptional transparency are demonstrated. Optimization was achieved by minimizing the phase separation during gelation, minimizing the light scattering, and yielding the exceptionally transparent aerogels. The aromatic PI backbone results in a high modulus while retaining a low thermal conductivities and high thermal stability. We demonstrate methods for inducing phase separation to increase the pore size and the effects on bulk properties. This study presents a better understanding of the route to producing transparent polymer aerogels.

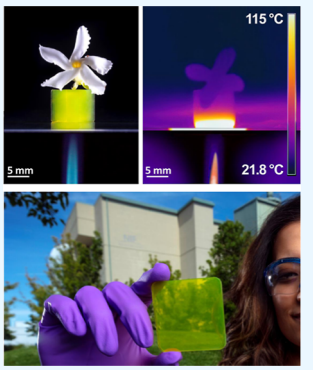

KEYWORDS: *aerogels, transparent, density, thermal insulator, surface area, polyimide, small-angle scattering*

INTRODUCTION

Aerogels are a diverse class of bottom-up porous materials with a wide range of applications. However, there is no strict porosity, composition, or synthetic process that defines an aerogel. Frequent characteristics include very high internal surface area, nanostructured porosity, and very low density (<1% ρ_{std}), and they are usually—though not exclusively—fabricated using supercritical drying.[1] They are among the lightest solid materials in the world and can exhibit various unique and desirable material properties.[2] Silica is the prototypical aerogel material and has been studied extensively; however, aerogels have been made from a vast array of materials, including metal oxides, carbon nanoparticles, inorganic colloids, and polymers with few limits on the composition.[3]

Polymeric aerogels combine the useful properties of aerogels, for example, high-surface area and low density, with the desirable properties of their polymeric constituents, for example, high strength, elasticity, shape memory, and chemical reactivity.[4] With a broad range of possible properties, novel combinations can be selected for complex applications. For example, polystyrene,[5] polyvinyl alcohol,[6] and polyacrylonitrile[7] aerogels can capture organic compounds such as dyes and oils for applications in oil spill remediation. Alternatively polyurea[8] and polybenzoxazine[9] aerogels exhibit exceptional mechanical performance. However, one downside of polymeric aerogels compared to their metal oxide counterparts is their low thermal stability, owing to the underlying chemistry of the polymeric backbone. Compared to their photogenic silica counterparts, polymer aerogels also tend to be opaque because of their larger feature sizes (primary particles, secondary particles, and pores). Transparent polymer aerogels would be exciting for optical applications, such as window insulators and transparent solar panels.[10] In this study, we demonstrate the synthesis of mechanically robust polyimide (PI) aerogels with high thermal stability and excellent transparency.

PIs are a family of polymers typically characterized by high thermal stability with deflection temperatures between 400 and 520 °C,[11,12] excellent chemical resistance,[13] low permittivity ($\varepsilon_r \sim 3-6$),[14] a low coefficient of thermal expansion (9×10^6–6×10^5 K^{-1}),[15] and high mechanical strength.[16] PI aerogels inherit these properties and have commercial applications as thermal insulators, catalyst supports, and filtration devices. Aromatic PI aerogels have previously been synthesized by gelation of chemically imidized PI in dilute solutions of <10 wt % using the classic reaction of dianhydride (PMDA) and 4,4′-methylenedianiline, followed by supercritical drying.[17] However, these aerogels often undergo significant shrinkage (up to 40%) and lack optical clarity. To improve the thermal stability

Received: June 7, 2022
Accepted: September 27, 2022

https://doi.org/10.1021/acsapm.2c00957
ACS Appl. Polym. Mater. XXXX, XXX, XXX−XXX

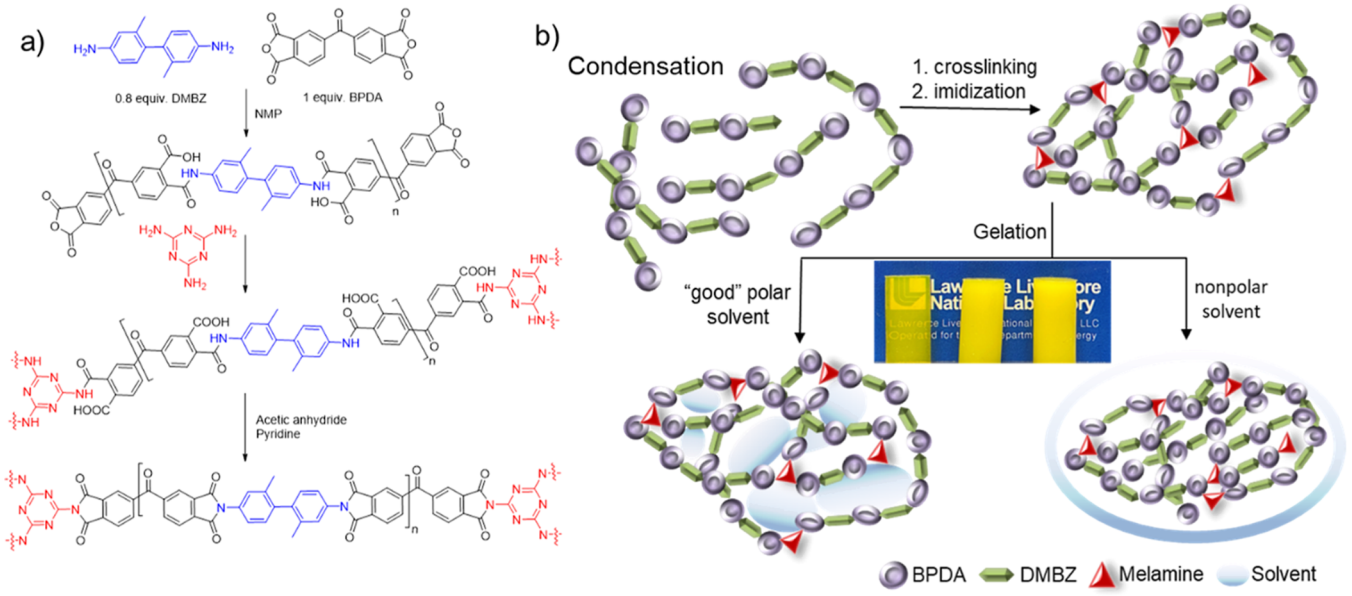

Figure 1. (a) Reaction conditions of PI aerogel used in this study and (b) proposed scheme of gelation steps for transparent and opaque PI aerogels. Inset: 2 cm molded aerogel cylinder with pure NMP, 25% toluene, and 50% toluene (left to right) after supercritical drying.

and minimize shrinking, other PI aerogels have been synthesized in dilute concentrations by cross-linking anhydride-capped polymeric acid oligomers through aromatic triamines including OAPS, TAB, and BTC.[12,18,19] Other also have shown the effect of an economical cross-linker such as melamine[20] varying concentrations and flexible backboned ODA.[20,21] However, these monolithic PI aerogels have generally been opaque.[22]

Judicious modification of the chemical structure of the PI chain of an aerogel can be used to subtly modify material properties. A highly aromatic backbone results in high thermal and mechanical stability due to strong chemical bonds and rigid, linear structure. Aliphatic and fluorinated constituents impart lower dielectric constants, hydrophobic properties, and flexibility due to the high degrees of rotational freedom in the aliphatic linker.[18,23] Bulkier monomers introduce steric effects which interrupt conjugation along the molecular chain, reducing color intensity. Charge-transfer complexes in fluorinated PIs formed between the alternating electron-poor CF_3 and electron-rich dianhydride also reduce color intensity.[24] However, sacrificing continuous conjugation due to the CF_3 substitution results in a reduction in stiffness.[25] These considerations provide guidance to optimizing PI aerogels for the desired material properties.

In this work, variation in melamine concentration, polymer concentration, solvent composition, and acetic anhydride (AA) mole ratios were investigated to produce mechanically robust, thermally stable, and highly transparent (>93% transmission) PI aerogels (Figure 1b-inset). The high transparency of PI aerogels is attributed to the combination of exceptionally small feature sizes: < 10 nm fibrous ligaments and <20 nm pores. We demonstrate that we can control pore volume and size, density, and opacity by modifying the polymer concentration and solvent composition. Critically, the use of a "good," polar solvent (*N*-methylpyrrolidone) prevents the phase separation of the polymer prior to gelation, resulting in a percolating network of small unimolecular fibers, minimizing optical scattering. Introducing a "bad," nonpolar solvent (toluene) induces solvent phase separation, resulting in optically scattering polymer-free voids with minimal effect on other nanoscale structures (Figure 1b).[26] While the melamine (cross-linker) concentration and use of excess AA (imidization agent) affected properties of the precursor sol, they did not have a significant effect on the resulting aerogel properties.

EXPERIMENTAL SECTION

Materials. 2,2′-Dimethyl-4,4′-diaminobiphenyl 98.0% (DMBZ), and 3,3′,4,4′-benzophenonetetracarboxylic dianhydride ≥96.0 (BPDA) were purchased from TCI. BPDA was used immediately once purchased to avoid discoloration with age. Melamine 99% was purchased from Across Organics. Pyridine. *N*-Methyl-2-pyrrolidone (NMP) and AA were purchased from VWR. All materials have been used as received.

General Characterization. A suite of complementary techniques was used to analyze the microstructures of the aerogels as a function of monomer concentration, cross-link density, and solvent composition. The effect of excess AA on gelation was also investigated.

Fabrication of PI Aerogel. Monolithic transparent aerogels were fabricated from sols with total solid concentrations in the range of 92−265 mg/mL. The polymer concentration is reported herein as milligram of solid monomers per milliliter of NMP unless otherwise noted. All the aerogels were prepared with a 1:0.8 ratio of BPDA to DMBZ and a standard of 0.03 equiv of melamine as a cross-linker. PI formulations are designated 0.8:1.0:*X*:7:*Y*, corresponding to the ratio of DMBZ/BPDA:melamine/pyridine:AA. In a typical preparation, DMBZ was fully dissolved in NMP before the addition of BPDA. Upon addition of BPDA, the solution was mixed for 1−7 min, depending on the polymer concentration. Longer mixing times were necessary for higher monomer concentrations. To cross-link the oligomers, a triamine cross-linker (melamine) was then added and mixed for 3 min. Disappearance of melamine solids indicates a reaction of melamine with the anhydride-terminated oligomers as melamine is only sparingly soluble in NMP. The mixture was then chemically imidized by the addition of AA and a weak base (pyridine), initiating gelation. This solution was mixed for 1−5 min, depending on gelation time, to achieve a homogeneous sol before molding. Higher polymer and/or cross-linker concentrations increased sol viscosity and required mechanical mixing (THINKY planetary mixer) to prevent macroscopic inhomogeneities in the final aerogels.

After the addition of AA, the homogeneous sol was molded in glass tubes or silicone rubber sealed with glass slides. 1 cm × 1 cm square

https://doi.org/10.1021/acsapm.2c00957
ACS Appl. Polym. Mater. XXXX, XXX, XXX−XXX

Table 1. Physical and Mechanical Properties of Aerogels at Various Polymer Concentrations, Using a 0.8:1.0:0.3:7:6 Formulation in NMP

polymer concentration (mg/mL)	measured density (mg/cm^3)	BET surface area (m^2/g)	Young's modulus (kPa)	transmission at 750 nm (%)	T_D (°C)
92	66.3 ± 2.3	688	312 ± 14	95	400
132	87.4 ± 3.2	794	470 ± 118	95	430
154	103.2 ± 2.8	660	1090 ± 110	90	400
231	147.7 ± 7.6	771	1780 ± 50	92	400
265	147.3 ± 5.3		1120 ± 80	92	420

Table 2. Data of Physical and Mechanical Properties of PI Aerogel with Variations in Cross-Linker Concentrations, Using a 0.8:1.0:*x*:7:6 Formulation at a Polymer Concentration of 132 mg/mL in NMP

cross-linker (melamine) (molar equiv)	measured density (mg/cm^3)	linear shrinkage (%)	BET surface area (m^2/g)	Young's modulus (kPa)	transmission at 750 nm (%)	T_D (°C)
0.00	79.7 ± 4.7	12%		337 ± 31		
0.01	77.2 ± 6.3	8%	616	281 ± 13	92	420
0.02	82.6 ± 1.7	10%	619	389 ± 99	88	320
0.03	87.4 ± 3.2	12%	794	470 ± 118	95	430
0.05	88.6 ± 2.9	12%		499 ± 43	91	440
0.10	83.0 ± 8.7	8%	638	392 ± 90	94	450

glass tubes (AdValue Technology) were used to produce samples for compression testing and density measurements. Discs were produced for small-angle X-ray scattering (SAXS), transparency, and thermal conductivity measurements by punching 1 cm diameter holes in 3 mm thick silicone rubber. All syntheses were performed in air at ambient pressures and temperatures. USAXS/SAXS measurements were performed under vacuum using Cu kα X-rays in a Xeuss 3.0 instrument (Xenocs).

Gels were aged for 24 h and then demolded for washing and solvent exchange. First, PI gels were immersed in 2× NMP for 24 h to remove unreacted monomers and excess AA. Subsequently, the gels were transferred to an NMP-acetone mixture (1:1) to gradually change the solvent and avoid pore collapse, then followed with 4 × 24 h exchanges in acetone to remove residual NMP. Finally, the samples were dried in a supercritical CO_2 dryer (EMS 3100) according to standard procedures. Approximately 10% linear shrinkage was typically observed during this drying process.

RESULTS AND DISCUSSION

Variations in melamine concentration, polymer concentration, solvent composition, and AA mole ratios were investigated to monitor their influence on bulk density, Young's modulus, opacity, and gelation time. The PI aerogel formulation that yielded the most promising properties (hereafter described as the model formulation) was synthesized with the 1:0.8:0.03:7:6 PI formulation at a concentration of 132 mg/mL NMP, as shown in Table 1. Aerogel samples from this formulation showed low light scattering with 95% transparency at 3 mm thicknesses. These materials possess a high-surface area measured by nitrogen sorption using the Brunauer–Emmett–Teller method (BET = 794 m^2/g) higher than many SiO_2 aerogel counterparts (BET = 595–749 m^2/g).[27] The model PI aerogel is easily handleable and possesses an elastic modulus of E_o = 473 kPa at a density of 87 mg/cm^3. These aerogels possess a thermal conductivity of 38 mW/m·K, and high thermal stability (T_D = 430 °C) comparable to other PI aerogels suitable for thermally stable insulation,[28] due to the conjugated PI backbone.

The addition of AA converts the soluble poly(amic acid) (PAA) to insoluble PI, driving gelation.[22] Table S1 shows the effect of AA concentrations on gelation time and physical characteristics of the aerogels. In gels with higher monomer concentration (132 mg/mL), PI tended to gel within 30 min. Increasing AA above 6 equiv in these gels showed little effect on gelation time as percolation is reached quickly during imidization with no significant changes in physical characteristics of the resulting aerogels. However, at a lower monomer concentration (e.g., 92 mg/mL), increasing AA sped up the final imidization dramatically and hence sped up gelation time from 100 min at 6 equiv to 40 min at 14 equiv. The increase in AA forced faster gelation without significantly changing pore or ligament size measured via SAXS, as shown in Figure S7a. AA concentrations below 6 molar equiv in either formulation failed to induce gelation, though extremely high polymer concentrations can gel without imidization. Increasing the concentration of the base catalyst, pyridine, did not noticeably affect the gelation time or physical properties of the aerogels.

We also investigated how changes in the polymer concentration affected the bulk density, opacity, gelation time, and Young's modulus of aerogels by using a 0.8:1.0:0.3:7:6 formulation with a constant cross-linker concentration of 0.3 molar equiv. By varying the polymer concentration from 92 to 265 mg/mL, as shown in Table 1, there was an increase in measured density from 66.3 to 150 mg/cm^3. However, the polymer concentration was observed to have minimal effect on aerogel transparency (>90%) and surface area (>660 m^2/g). Formulations with lower polymer concentrations possessed longer gelation times and lower viscosity. When polymer concentrations exceeded 265 mg/mL, the high viscosity of the solgel combined with fast gelation times (<1 min) yielded poorly mixed, visibly inhomogeneous aerogels with inconsistent mechanical properties (Table 2).

Furthermore, we investigated the impact of modifying the cross-linker (melamine) concentration on the aforementioned aerogel properties by using a 0.8:1.0:*x*:7:6 formulation at a polymer concentration of 132 mg/mL. Increased cross-linking density did not affect pore size or surface area measured by SAXS and BET (616–638 m^2/g), respectively (Figures S4a and S7b). Increasing cross-link density in the PI aerogels slightly increased their decomposition temperature (T_D) from 420 to 450 °C with little effect on transparency or BET surface area. The use of melamine above 0.10 molar equiv resulted in visibly inhomogeneous gels with inconsistent physical properties, similar to those resulting from high polymer concentrations. This appears to be due to a combination of increased

https://doi.org/10.1021/acsapm.2c00957
ACS Appl. Polym. Mater. XXXX, XXX, XXX–XXX

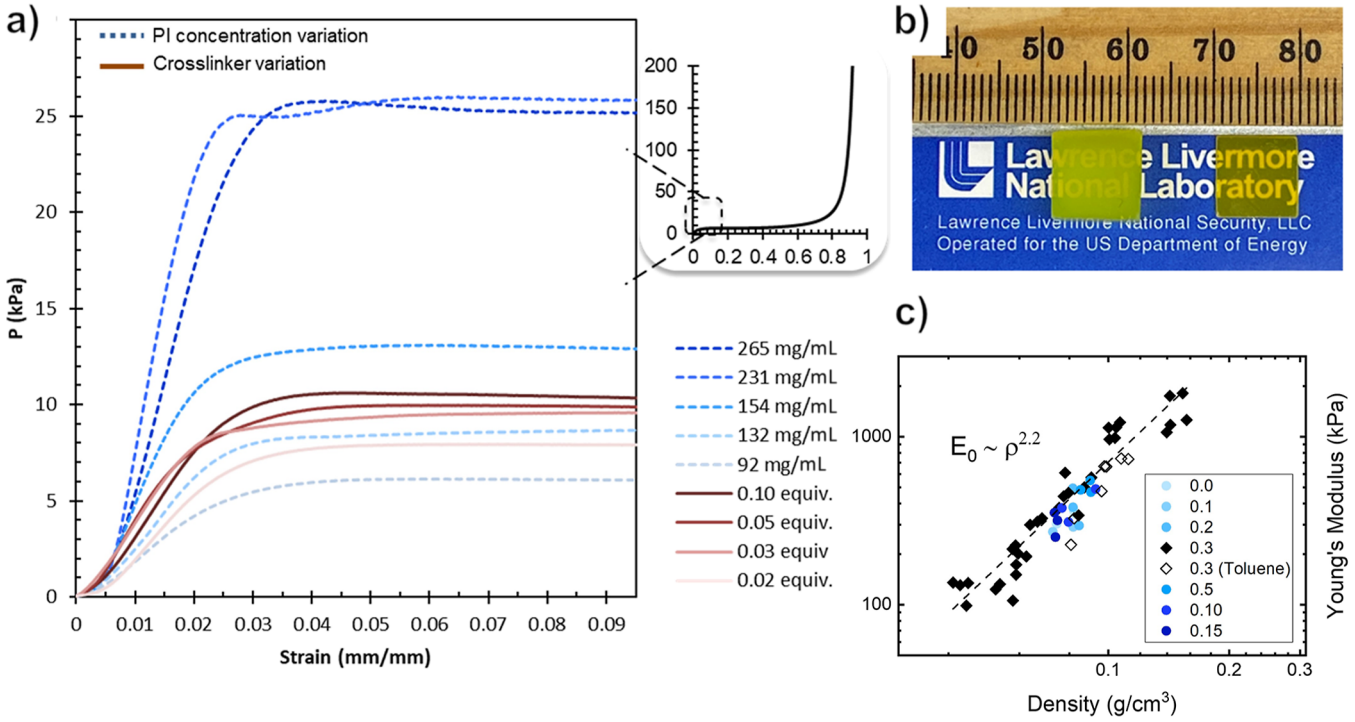

Figure 2. (a) Instron compression measuring strain and stiffness of the various PI aerogels with respect to density changes controlled by polymer concentration (dash lines) and cross-link concentration (solid lines) inset: example of full compression strain and stiffness curve. (b) Top view of 1 × 1 cm cube before and after compression showing no bulging or geometric distortion. (c) Log−log Ashby chart producing a linear fit (R = 0.90, and power of 2.22) in density and modulus for standard formulations (0.3 melamine). Nonstandard samples are labeled by melamine concentrations.

Table 3. Data of Physical and Mechanical Properties of PI Aerogels with Variations in the Polar-to-Nonpolar Solvent Ratio, Using a 0.8:1.0:0.03:7:6 Formulation at a Polymer Concentration of 132 mg/mL

solvent polarity variant	measured density (mg/cm^3)	shrinkage (%)	BET surface area (m^2/g)	Young's modulus (kPa)	transmission at 750 nm (%)	thermal conductivity (mW/m·K)
0% toluene	87.4	7%	794	472	95	38
10% toluene	88.8	9%	538	276	77	45
25% toluene	91.8	20%	641	600	66	
50% toluene	104.2	24%	592	737	36	46

sol viscosity and limitations of melamine solubility. Melamine solids remained visible even after extensive mixing and/or long (>3 h) reaction times prior to imidization.

Stress−strain curves from compression testing of transparent 1 × 1 cm PI aerogel cubes are shown in Figure 2a. The aerogels investigated have a modulus between 280 KPa and 1.25 MPa and yield stress between 5 and 25 kPa. For the model PI aerogel formulation, the measured density is 87.4 ± 2.6 mg/cm^3 with an elastic modulus of E_o = 473 kPa. The stress−strain curves of all the PI aerogels show similar deformation stages, starting with a linear elastic region up to ∼2% strain. The linear elastic region is followed by a plastic region up to >95% strain, characterized by a flat plateau up to ∼50% strain (as shown in Figure 2 inset), followed by stiffening as densification occurs. Due to the high porosity of the PI aerogels, no barreling was observed during compression, as shown in Figure 2b.

The exceedingly small feature sizes of both polymer nanofibers and pores minimize light scattering, yielding optically transparent aerogels. 3 mm PI aerogel disks possessed remarkably high transparency (>95%) in the visible region (540−790 nm) for all aerogels described above. However, the aerogels showed a clear color cutoff at ∼490 nm, yielding the characteristic yellow PI coloration. By adding increasing amounts of the poor, nonpolar solvent toluene at 0, 10, 25, and 50% by volume to NMP, opacity could be induced in PI aerogels (Table 3). Homogeneous PI gels could not be fabricated with more than 50% toluene due to insolubility of the synthesized PAA in those solvent mixtures. The total transmission of 3 mm thick aerogels formed in 50% toluene, as measured by UV−vis, was less than 35%. There was a monotonic increase in transmission with the decreasing toluene content, up to ∼95% total transmission in 100% NMP, as previously described.

While density is effectively unchanged from pure NMP to 10% toluene (86 and 88 mg/cm^3), a slight decrease in surface area and slight increase in modulus were observed and are shown in Table 3. Both formulations with pure NMP and mixtures of 50% toluene have similar fiber morphologies, as shown in transmission electron microscopy (TEM) (Figure 3a,b) with individual PI fiber diameters of 8.6 ± 2.6 nm. This morphology is notably distinct from the string-of-pearl

https://doi.org/10.1021/acsapm.2c00957
ACS Appl. Polym. Mater. XXXX, XXX, XXX−XXX

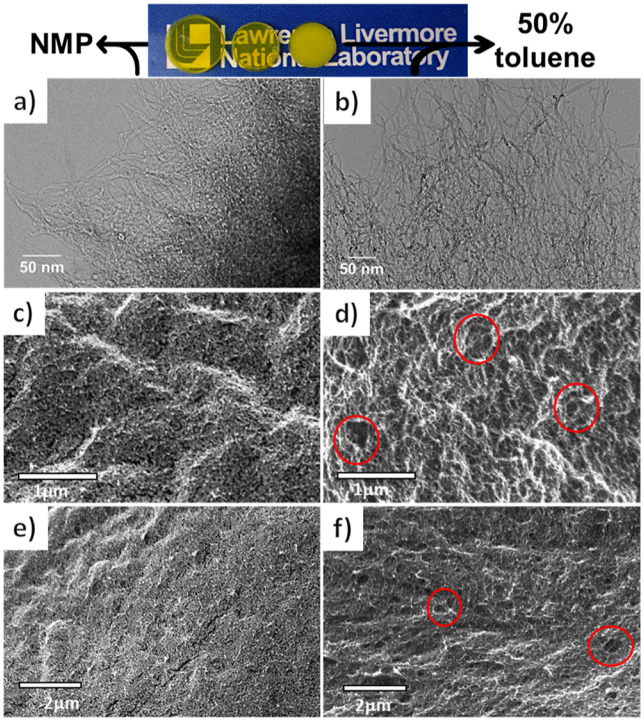

Figure 3. Inset: 1 cm diameter molded aerogel disks with pure NMP, 25% toluene, and 50% toluene (left to right) after supercritical drying showing relative transparency and shrinkage. TEM images of 0.8:1.0:03:7:6 PI aerogel formulations with 132 mg/mL polymer concentration in (a) NMP and (b) 50% toluene. SEM images at (c) 50,000× and (e) 25,000× magnification and 20 kV of 0.8:1.0:03:7:6 PI aerogel formulations with 132 mg/mL polymer concentration in NMP. SEM images at (d) 50,000× and (f) 25,000× magnification and 20 kV of 0.8:1.0:03:7:6 PI aerogel formulations with 132 mg/mL polymer concentration in 50% toluene.

structure, typically seen in PI aerogels.[22] While SEM cannot resolve individual fiber strands, it provides insights into the pore microstructure lacking in TEM images. SEM imaging of the interior section of PI aerogels (Figure 3c,d) shows a difference in the morphology of aerogels formed with pure NMP compared to those formed with 50% toluene. Specifically, the presence of voids (a few examples are circled in red) are only noticeable in PI aerogels made from the mixed solvent system, as shown in Figure 3d,f. The SEM images at lower magnification also suggest an increase in aggregation, or bundling, of polymer fibers in aerogels fabricated with 50% toluene compared with NMP.

While all aerogels experience measurable shrinkage after solvent exchange and supercritical drying, those fabricated from the solvent mixture undergo additional shrinkage during aging with syneresis not exhibited in gels fabricated in pure NMP, resulting in the most total shrinkage (up to 24%). Figure 3 inset shows 1 cm diameter molded aerogel disks with pure NMP, 25% toluene, and 50% toluene after supercritical drying. Nevertheless, the final aerogel material is chemically identical, as observed by solid-state ^{13}C NMR of PI aerogels (Figure S1) independent of the solvent composition. This is additionally supported by the fact that the T_D of the aerogels (a function of the chemical structure) is independent of the solvent composition. The thermal conductivity increases slightly from 38 to 45 mW/m·K, attributed to an increase in density and connectivity between the ligaments, increasing the component of thermal conductivity associated with the PI backbone. Aggregation of PI strands is further reflected by the decrease in internal surface area from 794 to 592 m^2/g with the addition of toluene. After accounting for changes in density due to shrinkage, the use of the mixed solvents had only a minor, if any, effect on the modulus of the aerogels.

While electron microscopy is a pivotal technique for identifying micro and nanostructures, it can suffer from sampling bias and is limited when analyzing complex 3D assemblies. In order to extract information about the size, shape, relative position, and volume fraction of the ligaments and pores, SAXS was collected and modeled in the q-range $0.006\ Å^{-1} < q < 1.5\ Å^{-1}$. Based on the TEM imaging, the solid ligaments have a mean diameter of ∼5 nm and aspect ratios greater than five. In short, ligaments were modeled as parallelepipeds (Figure 4a inset) with sides $\boldsymbol{A}$ and $\boldsymbol{B}$, corresponding to the short and long axis of a ligament cross-section, and length $\boldsymbol{C}$, corresponding to the straight-length segments of a ligament. Such segments can be terminated by the intersection with other ligaments or by a bend in the ligament attributed to degrees of freedom in the BPDA monomeric unit. The nestlike structure of the aerogels does not lend itself to a simple description of a pore shape, but an additional model feature corresponding to the through-space separation of ligaments ($\boldsymbol{L_p}$) captures the concept of pore size. In addition to the scattering from ligaments and pores, two diffraction peaks were observed in all the data, having peak positions, q_1 and q_2 of 0.640 and 1.255 Å, respectively; these positions correspond to d-spacings of 9.82 and 5.01 Å, respectively, attributing molecular order in the PI backbone. Additional details of the SAXS model is given in the Supporting Information.

From the SAXS modeling, ligaments have a minimum dimension $\boldsymbol{A} \approx 3$ nm (Table 4) with the second dimension ($\boldsymbol{B}$) typically a factor of 2 larger and statistically well separated from the other two features extracted by the model. The feature in the SAXS data unique to parallelepipeds is the intensity decay at $q > 0.1\ Å^{-1}$, which decays steeper than a Porod decay until $q \approx 0.2\ Å^{-1}$, where a faint knee-like feature and subsequent Porod decay are observed. A simple cylinder form-factor fails to describe the data in this region. The two smaller dimensions may be attributed to stacking effects, such as junction points where ligaments overlap or anisotropic assembly perpendicular to the length of the PI. Nevertheless, the two dimensions are consistent with the dimensions observed by TEM (Figure 3a,b). A significant change in the pore morphology with the addition of toluene to the solvent is captured by the feature size of ∼700 nm measured with USAXS (Figure 4d), corresponding to the large spheroidal pores primarily responsible for opacity. It only occurs with high (50%) toluene content that such large features can be observed in the USAXS region. Other changes in the aerogel morphology, that is, ligament size, spacing, and relative orientation, are contained at $-0.1\ Å^{-1} > q > 0.005\ Å^{-1}$, described in detail below.

However, the pore size (L_p) does change with density, the normalized standard deviation, $\sigma/\overline{A}$ is constant; therefore, there is no trend in the size of the ligaments ($\boldsymbol{A}$, $\boldsymbol{B}$) perpendicular to the $\boldsymbol{C}$-direction (length) or the stacking heterogeneity that results in a size distribution of pore changes with density. In all samples, a Guinier region is observed starting at $q \approx 0.01\ A^{-1}$. As the density goes down, ligaments become more disperse without changing size or shape, causing the distance between ligament intersections ($\boldsymbol{C}$) and interliga-

https://doi.org/10.1021/acsapm.2c00957
ACS Appl. Polym. Mater. XXXX, XXX, XXX−XXX

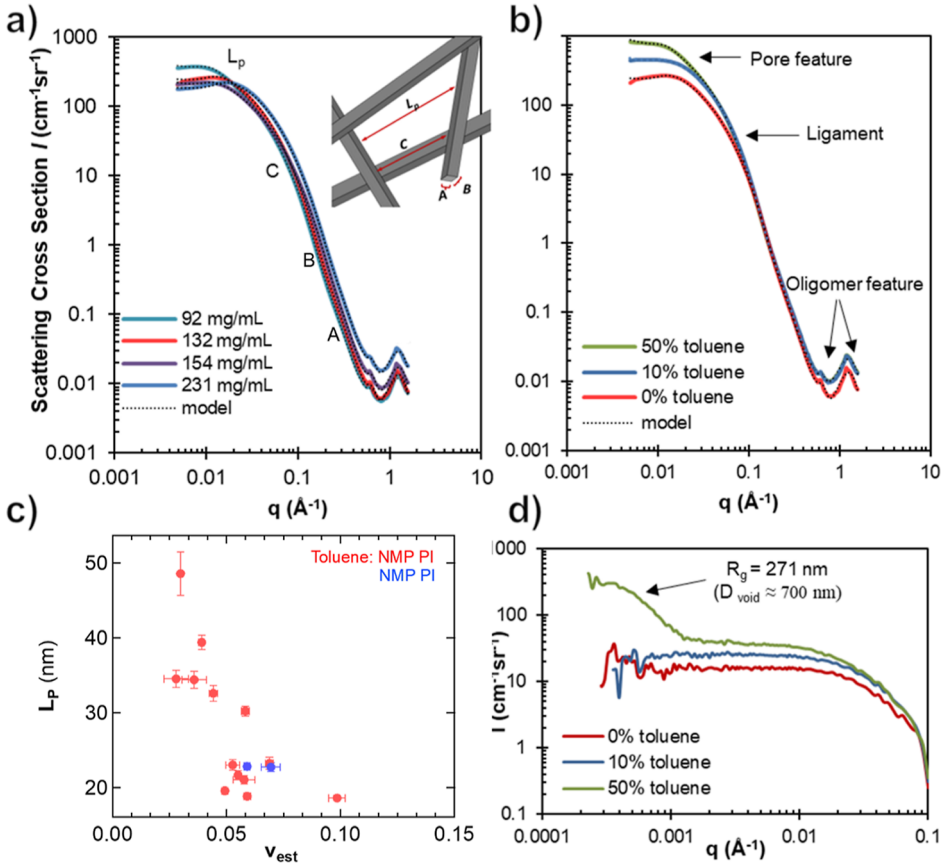

Figure 4. Log−log plots of the SAXS data (solid lines) with model fits of eq 1 from aerogels synthesized with different (a) polymer concentrations and (b) NMP/toluene ratios. Inset: illustration of the PI morphology. (c) Pore size of PI obtained from SAXS and density measurements. (d) Slit-smeared USAXS showing the presence of 700 nm features in the 50% toluene sample.

Table 4. Five Fit Parameters that Showed No Variation with Density for the PI Aerogels[a]

	$\bar{A}$ [nm]	B [nm]	$\sigma/\bar{A}$	$\sigma_d/\bar{d}$	b_g
mean ± max	2.9 ± 0.6	6.5 ± 1.2	0.32 ± 0.04	1.2 ± 0.3	0.002 ± 0.002

ment distances (L_p) to increase. Both of the scaling parameters associated with the diffraction peaks (k_1, k_2) from the PI increase linearly with density and PI volume fraction (v_{est}) (Figure S8), as expected. The relative intensity of scattering features associated with ligaments (*A*, *B*, *C*) in this region decreases (Figure 4b,c). Additionally, since the samples are mostly pore volume (interligament space), a decrease in density markedly reduces the relative volume fraction of ligaments, but only has a small effect on the volume fraction of pores.

[a]Values shown are averages obtained from sample-to-sample variations along with the maximum deviation observed.

The addition of toluene to the solvent composition has two distinct effects on the aerogel structure, as observed by SAXS. At high toluene concentrations, for example, 50%, a scattering feature is observed at low-q with diameter of ∼700 nm (Figure 4a,c), assuming a spherical shape.[29] The composition and volume fraction of these phases cannot be uniquely determined from the USAXS data; however, the large length scale is consistent with the high opacity of this sample and large round pores observed via SEM. A slight shift in intensity to lower q in the region dominated by ligament scattering suggests a slight increase in the aggregation of ligaments with increasing toluene concentrations, consistent with SEM.

The effect of synthetic parameters on the pore size distribution is arguably the most important parameter extracted from the SAXS data as it controls fluid-transfer properties critical in applications from catalysis to thermal insulation. It is difficult to characterize the pore morphology in random nanoporous materials via other common techniques such as electron microscopy and N_2 porosimetry. The relationship between the number density of pores, N_p, and the mean pore size, L_p, with total pore volume, $1 - v_{est}$, is estimated by the equation

$$\sum_p N_p L_p^3 \approx 1 - v_{est} \tag{1}$$

where the pore shape is approximated as a cube, though derived trends are expected to apply generally. We examine this behavior using the volume averaged pore size below. Two extremes of variation in the pore morphology with increasing pore volume are apparent from eq 1: (1) N_p remains constant and L_p increases linearly with $(1 - v_{est})^{1/3}$ and (2) the L_p is constant, and N_p increases linearly with $1 - v_{est}$. Based on the results from Figure S10, the number density of pores, N_p, *decreases* as the pore volume *increases*. L_p remains nearly constant at ≈175 ± 15 nm up to a pore volume fraction of ∼0.94, above which an increase in L_p is observed in the plot of

https://doi.org/10.1021/acsapm.2c00957
ACS Appl. Polym. Mater. XXXX, XXX, XXX−XXX

L_p versus $[1 - \nu_{est}]^{1/3}$ (Figure S10a). Therefore, it is most accurate to conceptualize growth in porosity as consolidation of pores, where they become larger but less numerous.

CONCLUSIONS

Mechanically robust, exceptionally transparent PI aerogels have been fabricated by optimizing three main aspects: high monomer concentration to minimize the pore size, the use of a rigid PI backbone, and minimizing the phase separation prior to gelation using a good solvent. While cross-linker concentration and imidization conditions altered the properties of the parent sol (namely, viscosity and gel time), they appeared to have little observable effect on the bulk properties of the resulting aerogels. The ability to modify nanomorphology without altering the underlying polymer chemistry during gel synthesis can be used to engineer nanoporous materials with the desired modulus, pore structure, and transparency. We fabricated exceptionally transparent aerogels, but by demonstrating a strategy for inducing opacity, we also demonstrated a general strategy for fabricating transparent aerogels for any polymer composition. Namely by preventing phase separation prior to gelation, both ligament and average pore size can be minimized.

In this study, PI phase separation is minimized using a good polar solvent and a rigid polymer to prevent molecular coiling. Introducing a poor nonpolar solvent such as toluene induces phase separation in two distinct forms: large voids formed by toluene-rich droplets separating from the PI-NMP-rich matrix and subtle changes to nanomorphology caused by PAA/PI phase separation from the NMP-toluene solvent mixture. Large droplet formation is specifically implicated here for the observed opacity. This strategy can be used to engineer hierarchical porosity in materials where transparency is not a necessary property.

SAXS measurements showed how pore morphology over multiple length scales changed as a function of aerogel density and solvent composition. Mass transport in porous media is a function of pore size, volume, and connectivity. While we were able to provide insights into the pore size distribution and volume as a function of synthetic parameters, we are unable to speak about pore connectivity and as such cannot accurately predict bulk mass transport properties. Additional experiments are underway to understand the effects of synthetic parameters and nanostructures on bulk transport properties in these PI aerogels.

ASSOCIATED CONTENT

Supporting Information

The Supporting Information is available free of charge at https://pubs.acs.org/doi/10.1021/acsapm.2c00957.

Aerogel foam fabrication, details on the experimental procedure and setup, SAXS modeling parameters and other supporting calculations, ^{1}H NMR of various foam compositions, UV−vis spectra, TGA data, BET data, and Instron compression of all composition mentioned in this study, and physical and mechanical properties of foam with various AA concentrations (PDF)

AUTHOR INFORMATION

Corresponding Author

Magi Y. Mettry − *Lawrence Livermore National Laboratory, Livermore, California 94550, United States;* orcid.org/0000-0001-5208-5032; Email: Yassa1@llnl.gov

Authors

Ariel M. Lighty − *Lawrence Livermore National Laboratory, Livermore, California 94550, United States;* orcid.org/0000-0002-5323-0921

Joshua A. Hammons − *Lawrence Livermore National Laboratory, Livermore, California 94550, United States;* orcid.org/0000-0003-0107-1954

Daniel R. Malone − *Lawrence Livermore National Laboratory, Livermore, California 94550, United States*

Kaila M. Bertsch − *Lawrence Livermore National Laboratory, Livermore, California 94550, United States*

Tyler M. Fears − *Lawrence Livermore National Laboratory, Livermore, California 94550, United States;* orcid.org/0000-0001-8648-7582

Complete contact information is available at: https://pubs.acs.org/10.1021/acsapm.2c00957

Author Contributions

M.Y.M. planned, executed the research, and provided the overall direction under the supervision of T.M.F. A.M.L. conducted PI synthesis. J.A.H. lead USAXS and SAXS measurements. D.R.M. conducted PI postprocess and mechanical measurements. K.M.B. conducted TEM imaging. The manuscript was written through contributions of all authors. All authors have given approval to the final version of the manuscript.

Funding

Funding was available under LDRD project number 21-ERD-010 (IM release #LLNL-JRNL-828326).

Notes

The authors declare no competing financial interest.

ACKNOWLEDGMENTS

The authors gratefully acknowledge Maxwell A.T. Marple for assistance with NMR measurements. The work was conducted under the auspices of the U.S. Department of Energy by Lawrence Livermore National Laboratory under contract DE-AC52-07NA27344.

REFERENCES

(1) (a) Pajonk, G. M. Aerogel Catalysts. *Appl. Catal.* **1991**, *72*, 217−266. (b) Pajonk, G. M.; Rao, A. V.; Pinto, N.; Ehrburger-Dolle, F.; Gil, M. B. Monolithic carbon aerogels for fuel cell electrodes. *Stud. Surf. Sci. Catal.* **1998**, *118*, 167−174. (c) Pajonk, G. M. Transparent silica aerogels. *J. Non-Cryst. Solids* **1998**, *225*, 307−314. (d) Pekala, R. W.; Farmer, J. C.; Alviso, C. T.; Tran, T. D.; Mayer, S. T.; Miller, J. M.; Dunn, B. Carbon aerogels for electrochemical applications. *J. Non-Cryst. Solids* **1998**, *225*, 74−80. (e) Pekala, R. W.; Schaefer, D. W. Structure of Organic Aerogels .1. Morphology and Scaling. *Macromolecules* **1993**, *26*, 5487−5493.

(2) Hüsing, N.; Schubert, U. Aerogels airy materials: Chemistry, structure, and properties. *Angew. Chem., Int. Ed.* **1998**, *37*, 22−45.

(3) (a) Fears, T. M.; Hammons, J. A.; Sain, J. D.; Nielsen, M. H.; Braun, T.; Kucheyev, S. O. Ultra-low-density silver aerogels via freeze-substitution. *APL Mater.* **2018**, *6*, 091103. (b) Baumann, T. F.; Gash, A. E.; Chinn, S. C.; Sawvel, A. M.; Maxwell, R. S.; Satcher, J. H. Synthesis of high-surface-area alumina aerogels without the use of alkoxide precursors. *Chem. Mater.* **2005**, *17*, 395−401. (c) Baumann,

T. F.; Satcher, J. H. Template-directed synthesis of periodic macroporous organic and carbon aerogels. *J. Non-Cryst. Solids* **2004**, *350*, 120−125. (d) Worsley, M. A.; Shin, S. J.; Merrill, M. D.; Lenhardt, J.; Nelson, A. J.; Woo, L. Y.; Gash, A. E.; Baumann, T. F.; Orme, C. A. Ultra low Density, Monolithic WS2, MoS2, and MoS2/Graphene Aerogels. *ACS Nano* **2015**, *9*, 4698−4705. (e) Tian, H. Y.; Buckley, C. E.; Wang, S. B.; Zhou, M. F. Enhanced hydrogen storage capacity in carbon aerogels treated with KOH. *Carbon* **2009**, *47*, 2128−2130. (f) Worsley, M. A.; Stadermann, M.; Wang, Y. M. M.; Satcher, J. H., Jr.; Baumann, T. F. High surface area carbon aerogels as porous substrates for direct growth of carbon nanotubes. *Chem. Commun.* **2010**, *46*, 9253−9255. (g) Zhao, L.; Bhatia, B.; Yang, S.; Strobach, E.; Weinstein, L. A.; Cooper, T. A.; Chen, G.; Wang, E. N. Harnessing Heat Beyond 200 °C from Unconcentrated Sunlight with Nonevacuated Transparent Aerogels. *ACS Nano* **2019**, *13*, 7508−7516.

(4) Ghaffari-Mosanenzadeh, S.; Aghababaei Tafreshi, O. A.; Karamikamkar, S.; Saadatnia, Z.; Rad, E.; Meysami, M.; Naguib, H. E. Recent advances in tailoring and improving the properties of polyimide aerogels and their application. *Adv. Colloid Interface Sci.* **2022**, *304*, 304.

(5) (a) Wang, X.; Jana, S. C. Synergistic hybrid organic-inorganic aerogels. *ACS Appl. Mater. Interfaces* **2013**, *5*, 6423−6429. (b) Wang, X.; Jana, S. C. Tailoring of morphology and surface properties of syndiotactic polystyrene aerogels. *Langmuir* **2013**, *29*, 5589−5598.

(6) Xiao, J. L.; Zhang, J. F.; Lv, W. Y.; Song, Y. H.; Zheng, Q. Multifunctional graphene/poly(vinyl alcohol) aerogels: In situ hydrothermal preparation and applications in broad-spectrum adsorption for dyes and oils. *Carbon* **2017**, *123*, 354−363.

(7) Feng, J. Z.; Zhang, C. R.; Feng, J.; Jiang, Y. G.; Zhao, N. Carbon Aerogel Composites Prepared by Ambient Drying and Using Oxidized Polyacrylonitrile Fibers as Reinforcements. *ACS Appl. Mater. Interfaces* **2011**, *3*, 4796−4803.

(8) (a) Lee, J. K.; Gould, G. L.; Rhine, W. Polyurea based aerogel for a high performance thermal insulation material. *J. Sol-Gel Sci. Technol.* **2009**, *49*, 209−220. (b) Nguyen, B. N.; Scheiman, D. A.; Meador, M. A. B.; Guo, J.; Hamilton, B.; McCorkle, L. S. Effect of Urea Links in the Backbone of Polyimide Aerogels. *ACS Appl. Polym. Mater.* **2021**, *3*, 2027−2037.

(9) Mahadik-Khanolkar, S.; Donthula, S.; Bang, A.; Wisner, C.; Sotiriou-Leventis, C.; Leventis, N. Polybenzoxazine Aerogels. 2. Interpenetrating Networks with Iron Oxide and the Carbothermal Synthesis of Highly Porous Monolithic Pure Iron(0) Aerogels as Energetic Materials. *Chem. Mater.* **2014**, *26*, 1318−1331.

(10) Husain, A. A. F.; Hasan, W. Z. W.; Shafie, S.; Hamidon, M. N.; Pandey, S. S. A review of transparent solar photovoltaic technologies. *Renewable Sustainable Energy Rev.* **2018**, *94*, 779−791.

(11) Guo, H.; Meador, M. A.; McCorkle, L.; Quade, D. J.; Guo, J.; Hamilton, B.; Cakmak, M.; Sprowl, G. Polyimide aerogels cross-linked through amine functionalized polyoligomeric silsesquioxane. *ACS Appl. Mater. Interfaces* **2011**, *3*, 546−552.

(12) Guo, H. Q.; Meador, M. A. B.; McCorkle, L.; Quade, D. J.; Guo, J.; Hamilton, B.; Cakmak, M. Tailoring Properties of Cross-Linked Polyimide Aerogels for Better Moisture Resistance, Flexibility, and Strength. *ACS Appl. Mater. Interfaces* **2012**, *4*, 5422−5429.

(13) (a) Cherkashina, N. I.; Pavlenko, V. I.; Manaev, V. A.; Kuprieva, O. V.; Kashibadze, N. V.; Samoilova, E. S. Multilayer coatings based on polyimide track membranes and nanodispersed lead. *Prog. Org. Coat.* **2020**, *138*, 105432. (b) Yanagishita, H.; Kitamoto, D.; Haraya, K.; Nakane, T.; Okada, T.; Matsuda, H.; Idemoto, Y.; Koura, N. Separation performance of polyimide composite membrane prepared by dip coating process. *J. Membr. Sci.* **2001**, *188*, 165−172.

(14) Couderc, S.; Ducloux, O.; Kim, B. J.; Someya, T. A mechanical switch device made of a polyimide-coated microfibrillated cellulose sheet. *J. Micromech. Microeng.* **2009**, *19*, 055006.

(15) (a) Yang, Z. H.; Ma, P. C.; Li, F. R.; Guo, H. Q.; Kang, C. Q.; Gao, L. X. Ultrahigh thermal-stability polyimides with low CTE and required flexibility by formation of hydrogen bonds between poly(amic acid)s. *Eur. Polym. J.* **2021**, *148*, 110369. (b) Liu, F. Y.; Liu, Z. H.; Gao, S. Y.; You, Q. L.; Zou, L. Y.; Chen, J.; Liu, J. Y.; Liu, X. Q. Polyimide film with low thermal expansion and high transparency by self-enhancement of polyimide/SiC nanofibers net. *RSC Adv.* **2018**, *8*, 19034−19040.

(16) Ni, H. J.; Liu, J. G.; Wang, Z. H.; Yang, S. Y. A review on colorless and optically transparent polyimide films: Chemistry, process and engineering applications. *J. Ind. Eng. Chem.* **2015**, *28*, 16−27.

(17) Chidambareswarapattar, C.; Larimore, Z.; Sotiriou-Leventis, C.; Mang, J. T.; Leventis, N. One-step room-temperature synthesis of fibrous polyimide aerogels from anhydrides and isocyanates and conversion to isomorphic carbons. *J. Mater. Chem.* **2010**, *20*, 9666−9678.

(18) Meador, M. A. B.; McMillon, E.; Sandberg, A.; Barrios, E.; Wilmoth, N. G.; Mueller, C. H.; Miranda, F. A. Dielectric and Other Properties of Polyimide Aerogels Containing Fluorinated Blocks. *ACS Appl. Mater. Interfaces* **2014**, *6*, 6062−6068.

(19) Feng, J.; Wang, X.; Jiang, Y.; Du, D.; Feng, J. Study on Thermal Conductivities of Aromatic Polyimide Aerogels. *ACS Appl. Mater. Interfaces* **2016**, *8*, 12992−12996.

(20) Liu, S.; Chen, W. W.; Zhou, X. M. Polyimide aerogels using melamine as an economical yet effective crosslinker. *J. Porous Mater.* **2021**, *28*, 1155−1165.

(21) Tafreshi, O. A.; Ghaffari-Mosanenzadeh, S.; Karamikamkar, S.; Saadatnia, Z.; Kiddell, S.; Park, C. B.; Naguib, H. E. Novel, flexible, and transparent thin film polyimide aerogels with enhanced thermal insulation and high service temperature. *J. Mater. Chem. C* **2022**, *10*, 5088−5108.

(22) Chen, W.; Zhou, X.; Wan, M.; Tang, Y. Recent progress on polyimide aerogels against shrinkage: a review. *J. Mater. Sci.* **2022**, *57*, 13233.

(23) Hong, J. I.; Winberg, P.; Schadler, L. S.; Siegel, R. W. Dielectric properties of zinc oxide/low density polyethylene nanocomposites. *Mater. Lett.* **2005**, *59*, 473−476.

(24) Dine-Hart, R. A.; Wright, W. W. Study of Some Properties of Aromatic Imides. *Makromol. Chem.* **1971**, *143*, 189.

(25) Vivod, S. L.; Meador, M. A. B.; Pugh, C.; Wilkosz, M.; Calomino, K.; McCorkle, L. Toward Improved Optical Transparency of Polyimide Aerogels. *ACS Appl. Mater. Interfaces* **2020**, *12*, 8622−8633.

(26) (a) Chen, M.Fundamental properties of colloidal unimolecular polymer particles. Ph.D. Thesis, Missouri University of Science and Technology, 2013. (b) Anderson, M. L.; Morris, C. A.; Stroud, R. M.; Merzbacher, C. I.; Rolison, D. R. Colloidal Au aerogels: Preparation, properties, and characterization. *Langmuir* **1999**, *15*, 674. (c) Onsager, L. The Effects of Shape on the Interaction of Colloidal Particles. *Ann. N. Y. Acad. Sci.* **1949**, *51*, 627−659.

(27) (a) Kanamori, K.; Aizawa, M.; Nakanishi, K.; Hanada, T. New transparent methylsilsesquioxane aerogels and xerogels with improved mechanical properties. *Adv. Mater.* **2007**, *19*, 1589. (b) Wu, X. D.; Shao, G. F.; Shen, X. D.; Cui, S.; Chen, X. B. Evolution of the novel C/SiO2/SiC ternary aerogel with high specific surface area and improved oxidation resistance. *Chem. Eng. J.* **2017**, *330*, 1022−1034.

(28) Yu, Z. L.; Yang, N.; Apostolopoulou-Kalkavoura, V.; Qin, B.; Ma, Z. Y.; Xing, W. Y.; Qiao, C.; Bergström, L.; Antonietti, M.; Yu, S. H. Fire-Retardant and Thermally Insulating Phenolic-Silica Aerogels. *Angew. Chem., Int. Ed. Engl.* **2018**, *57*, 4538−4542.

(29) Glatter, O.; Kratky, O.*Small Angle X-Ray Scattering*; Academic Press, 1982.

https://doi.org/10.1021/acsapm.2c00957
ACS Appl. Polym. Mater. XXXX, XXX, XXX−XXX